

Studies on Dielectric, Electrical, Magnetic and Hetero-photocatalytic Properties of Bismuth Layered Aurivillius Oxides



Thesis submitted in partial fulfilment

For the Award of Degree

DOCTOR OF PHILOSOPHY

By

SHRUTI SINGH

DEPARTMENT OF CHEMISTRY

INDIAN INSTITUTE OF TECHNOLOGY

(BANARAS HINDU UNIVERSITY)

VARANASI-221005


Roll No.: 17051011

2022

CERTIFICATE

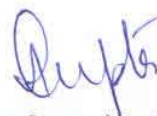
It is certified that the work contained in the thesis titled "**Studies on dielectric, electrical, magnetic and hetero-photocatalytic properties of Bismuth Layered Aurivillius Oxides**" by "**Shruti Singh**" has been carried out under my supervision and that this work has not been submitted elsewhere for a degree.

It is further certified that the student has fulfilled all the requirements of Comprehensive examination, Candidacy and SOTA for the award of Ph.D. degree.



23/6/2022

Prof. K. D. Mandal (Supervisor)
Department of Chemistry
Indian Institute of Technology
(Banaras Hindu University) Varanasi



Dr. Asha Gupta (Co-Supervisor)
Department of Chemistry
Indian Institute of Technology
(Banaras Hindu University) Varanasi

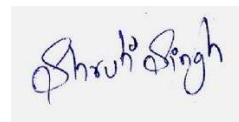
DECLARATION BY THE CANDIDATE

I, Shruti Singh, certify that the work embodied in this thesis is my own bonafide work and carried out by me under the supervision of Prof. K. D. Mandal from 2017 to 2022, at the Department of Chemistry, Indian Institute of Technology (Banaras Hindu University), Varanasi. The matter embodied in this thesis has not been submitted for the award of any other degree/diploma.

I declare that I have faithfully acknowledged and given credits to the research workers wherever their works have been cited in my work in this thesis. I further declare that I have not deliberately copied any other's work, paragraphs, text, data, results, etc., reported in journals, books, magazines, reports dissertations, theses, etc., or available at websites and have not included them in this thesis and have not cited as my own work.

Date: 23/06/2022

Place: Varanasi



(Shruti Singh)

COPYRIGHT TRANSFER CERTIFICATE

Title of the Thesis: Studies on dielectric, electrical, magnetic and hetero-photocatalytic properties of Bismuth Layered Aurivillius Oxides.

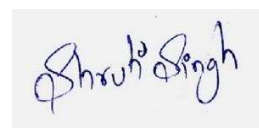
Name of the Student: Shruti Singh

Copyright Transfer

The undersigned hereby assigns to the Indian Institute of Technology (Banaras Hindu University) Varanasi all rights under copyright that may exist in and for the above thesis submitted for the award of the “Doctor of Philosophy”.

Date: 23/06/2022

Place: Varanasi



Signature of the Student
(Shruti Singh)

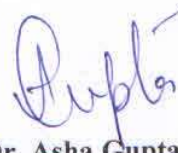
Note: However, the author may reproduce or authorize others to reproduce material extracted verbatim from the thesis or derivative of the thesis for the author’s personal use provided that the source and the Institute’s copyright notice are indicated.

CERTIFICATE BY THE SUPERVISOR(S)

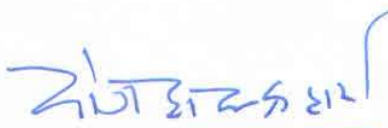
It is certified that the above statement made by the student is correct to the best of my knowledge.


23/6/2022

Prof. K. D. Mandal
(Supervisor)
Department of Chemistry
Indian Institute of Technology
(Banaras Hindu University)
Varanasi



Dr. Asha Gupta
(Co-supervisor)
Department of Chemistry
Indian Institute of Technology
(Banaras Hindu University)
Varanasi



Prof. Y.C. Sharma
(Head)
Department of Chemistry
Indian Institute of Technology
(Banaras Hindu University)
Varanasi

विभागाध्यक्ष / HEAD
रसायन विज्ञान विभाग
Department of Chemistry
भारतीय प्रौद्योगिकी संस्थान (का.हि.वि.वि.)
Indian Institute of Technology (B.H.U.)
वाराणसी-221005/Varanasi



***Dedicated To My
Parents***

ACKNOWLEDGMENTS

World in today's scenario is running in high pace, making it hard to accomplish a goal without support of each other. Today, at the acme of my thesis, with full heart, I gratefully remember those supports: as one flower makes no garland, this research would not have taken shape without their involvement.

Foremost, I would like to express my heartfelt gratitude to my supervisor **Prof. K. D. Mandal**, Department of Chemistry, Indian Institute of Technology, (B.H.U) for allowing me to join his research group, and for providing the precursor base knowledge for my research. Through his unflinching support, constructive criticism, his scientific intuition and advice, he exceptionally inspired me and enriched my growth as a researcher. His involvement nourished my intellectual maturity, provided me opportunities to collaborate with other scientists, that going to help me throughout my career.

With great humility, I acknowledge the kind patronage, loving inspiration and timely guidance, which I received from my Co-Supervisor **Dr. Asha Gupta**, Department of Chemistry, Indian Institute of Technology, (B.H.U).

I would to express my gratefulness to **Prof. Y.C. Sharma** Head, Department of Chemistry, Indian Institute of Technology, (B.H.U) Varanasi for providing research facilities available in the Department.

I would like to express my sincere thanks to my RPEC members **Dr. Indrajit Sinha**, Department of Chemistry, IIT (B.H.U) Varanasi and **Dr. Preetam Singh**, Department of Ceramic, I.I.T (B.H.U) Varanasi for always keeping me on my toe.

Enough encouragement and knowledge have been imparted to me by the faculty members of the department during course work session and in the path of research. I will forever be indebted to them.

ACKNOWLEDGMENTS

I would also like to acknowledge the In-charge and members of the central instrumentation facility centre (CIFC) for extending me instrumental facilities and office staff of the Chemistry Department for always keeping paperwork ready before hand. I wish to express my special thanks to IIT (BHU) for providing financial support to carry out this work.

I am also thankful to my seniors, Late Dr. Ankur Khare, Dr. Pooja Gautam, Dr. Atendra Kumar and Dr. Vinod Kumar and existing lab mates for their constant help and support.

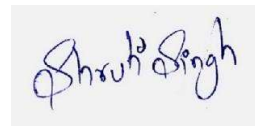
This acknowledgement would be incomplete without mentioning my loving friends **Dr. Sukinsu Kanan** and **Shweta Agrawal** for their invaluable help, love and moral support. Special mention to my friend **Late Tanu Singh**, who has been my greatest support throughout this journey.

I would like to express my eternal appreciation towards my parents **Mr. Rajendra Singh and Mrs. Satyavati Singh** and siblings; **Dr. Prannav Satyaraj, Mrs. Surabhi Singh and Mrs. Shuchi Singh**, who have supported me in every thick and thin with unconditional love and patience.

With regards to numerous questions about my future academic endeavours, I shall answer in the words of *Sir Winston Churchill*, “Now, this is not the end. It is not even the beginning of the end. But it is, perhaps, the end of the beginning.”

Place: Varanasi

Date: 23/06/2022



Shrut Singh

Content	Page No.
Title of Thesis	i
Certificate	ii
Declaration by the Candidate	iii
Certificate by the Supervisor(s)	iv
Copyright Transfer Certificate	v
Dedication	vi
Acknowledgment	vii-viii
Contents	ix-xv
List of Figures	xvi-xxi
List of Tables	xxii-xxiii
List of symbols/ Abbreviation	xxiv-xxv
Preface	xxvi-xxxi
Chapter 1	1-52
1.1 History of Perovskite	1
1.2 High dielectric constant ABO₃ Perovskite	2
(a) Calcium Titanate CaTiO₃	2
(b) Barium Titanate (BaTiO₃)	2
(c) Strontium Titanate SrTiO₃	4

1.3 Perovskite Structure and Derivatives	6
1.3.1 Cubic Perovskites	6
1.3.2 Complex perovskite	7
(a) Double Perovskites	8
(b) Layered Perovskites: Ruddleson-Popper, Aurivillius and Dion- Jacobson phases	8
1.4 Applications of Perovskites Oxides:	12
1.5 Ceramic Materials	15
1.6 Composite Materials	15
1.7 Capacitors	16
1.8 Dielectric materials	18
1.9 Types of Polarization	19
1.9.1 Electronic or Atomic Polarization	19
1.9.2 Ionic Polarization	19
1.9.3 Dipolar or Orientation Polarization	20
1.9.4 Interface or Space Charge Polarization:	20
1.10 Dielectric Constant	22
1.11 Dielectric loss	23

1.12 Impedance	25
1.13 Ferroelectricity	27
1.14 Magnetic Properties	30
1.14.1 Origin of magnetism	32
1.14.2 Magnetic Domain	33
1.14.3 Hysteresis loop	35
1.15 Dye Degradation an Overview	37
1.15.1 Mechanism of Photocatalytic Dyes Degradation	39
1.15.2 Photocatalysts used in Dyes Degradation	41
1.16 Aim of the present work	43
1.17 References	46
Chapter 2	53-73
2.1 Materials Design and methods for the synthesis and characterization	53
2.2 Material used	54
2.3 Calcination Process	56
2.4 Sintering Process	57

2.5 Techniques for characterization of synthesized ceramic materials:	57
2.5.1 Phase and Crystal Structure Analysis	57
2.5.2 Scanning Electron Microscopy (SEM) Analysis	60
2.5.3 Energy Dispersive X-ray Spectroscopy (EDX)	62
2.5.4 Transmission Electron Microscopy (TEM) Analysis	62
2.5.5 Atomic force microscopy	64
2.5.6 Superconducting quantum interference device (SQUID)	65
2.5.7 Electric and Dielectric Measurement:	66
2.5.8 Impedance and Conductivity	68
2.5.9 Automatic PE loop tracer	68
2.5.10 Malvern Zetasizer Nano ZS	69
2.5.11 Brunauer–Emmett–Teller (BET) theory	70
2.6 References	72
Chapter 3	74-112
3.1 Introduction	74
3.2 Experimental Section	77
3.2.1 Photocatalytic Experiment	78
3.3 Characterization	79

3.4 Results and Discussion	80
3.5 Magnetic studies	90
3.6 Electrical and Impedance studies	92
3.7 Dielectric Studies	99
3.8 Bandgap Analysis	103
3.9 BET Surface Area Analysis	104
3.10 Photocatalytic efficiency	105
3.11 References	108
Chapter 4	113-149
4.1 Introduction	113
4.2 Experimental Section	117
4.2.1 Photocatalytic Experiment	117
4.3 Characterization	118
4.4 Results and Discussion	119
4.5 Magnetic studies	129

4.6 Impedance studies	130
4.7 Dielectric Studies	135
4.8 Bandgap Analysis	139
4.9 BET Surface Area Analysis	140
4.10 Photocatalytic efficiency	141
4.11 References	144
Chapter 5	150-180
5.1 Introduction	150
5.2 Experimental Section	152
5.2.1 Photocatalytic Experiment	153
5.3 Characterization	153
5.4 Results and Discussion	154
5.5 Magnetic studies	162
5.6 Impedance studies	164

5.7 Dielectric Studies	168
5.8 Bandgap Analysis	171
5.9 BET Surface Area Analysis	172
5.10 Photocatalytic efficiency	174
5.11 References	177
Conclusions	181-183
List of Publications	184-187

Figure 1.1 shows the Perovskite structure (Rabuffetti and Brutchey 2014)	2
Figure 1.2 Phase diagram for conversion of BaTiO ₃ Perovskite structure	3
Figure 1.3 shows the cubic Perovskite structure of SrTiO ₃ .	7
Figure 1.4 shows the double perovskite structure of Sr ₂ FeMoO ₆ .	9
Figure 1.5 shows the n=1 in Sr ₂ RuO ₄ and n=2 in Sr ₃ Ru ₂ O ₇ Ruddleson-Popper phases structure.	10
Figure 1.6 shows Aurivillius phases structure of is Bi ₃ TiNbO ₉ , where n=2.	11
Figure 1.7 shows of CsLaNb ₂ O ₇ Dion-Jacobson phase structure.	12
Figure 1.8 Parallel plate capacitor with the plates separated by distance (d) and area of each plate (A).	17
Figure 1.9 (a)non- polarized plates and (b) polarized and of an applied electric field.	19
Figure 1.10 Schematic figures between dielectric constant vs log (frequency) showing various mechanisms	20
Figure 1.11 Complex plot of impedance plane and its equivalent circuit	27
Figure 1.12 PE hysteresis loop	28
Figure 1.13 P-E hysteresis loops for BaTiO ₃ above and below the Curie temperature (T _c)	29
Figure 1.14 Flow chart for the origin of magnetism in the materials.	33
Figure 1.15 Hysteresis loop or B-H curve	35
Figure 1.16 shows the M-H hysteresis curve for paramagnetism, superparamagnetism, and ferromagnetism.	37
Figure 1.17 The pictorial representation of Photocatalytic Dyes Degradation.	41
Figure 2.1 Flow chart for the synthesis of materials by chemical route.	56

Figure 2.2 Powder XRD instrument, RigakuMiniflex600 (Japan)	58
Figure 2.3 Braggs law of X-ray diffraction	59
Figure 2.4 Scanning Electron microscopy (SEM, ZEISS model, EVO18 Germany) attached with EDX Analysis instrument (Oxford instrument; USA)	61
Figure 2.5 Signal produced near the surface of specimen due to interaction with electron beam.	63
Figure 2.6 Transmission electron microscope (TEM, FEI Tecnai-20G ²)	64
Figure 2.7 Superconducting quantum interference devices (SQUID) (Quantum Design, MPMS 3)	66
Figure 2.8 LCR Meter (PSM 1735, Newton 4th Ltd, U.K.) used for dielectric measurement	67
Figure 2.9 Sawyer-Tower circuit	69
	69
Figure 2.10 Malvern Zetasizer Nano ZS (Particle Size Analyzer)	
Figure 2.11 Brunauer–Emmett–Teller (BET)	70
Figure 3.1 indicates high-resolution x-ray diffraction (HR-XRD) patterns of BTO-BT nanocomposite sintered at 900 °C for 8 h.	80
Figure 3.2 Le-Bail fitting of BTO-BT nanocomposite, in which black line represents calculated data, the red line indicates experimental observed data and the blue line represents the difference between observed and calculated (($Y_{cal} - Y_{obs}$) data.	81
Figure 3.3 FT-IR spectra BTO-BT nanocomposite.	83
Figure 3.4 (a) SAED patterns (b) HR-TEM images showing d-spacing, and (c) Bright Field TEM Images of BTO-BT nanocomposite	84
Figure 3.5 (a) SEM micrograph, and (b) EDX spectra of BTO-BT nanocomposite.	85
Figure 3.6 Particle size distribution of BTO-BT nanocomposite	86
Figure 3.7 Zeta potential distribution of BTO-BT nanocomposite	86
Figure 3.8 (a) Histogram graph for the particle size distribution, (b) 2-D watershed images for grain boundary and (c) 3-D for surface roughness of BTO-BT nanocomposite.	88

Figure 3.9(a)–(d) High-resolution XPS spectra of the BTO-BT nanocomposite.	89
Figure 3.10. Temperature-dependent ZFC and FC at H= 100 Oe BTO-BT nanocomposite.	90
Figure 3.11 M-H hysteresis loop from 5 K to 300 K for BTO-BT nanocomposite.	92
Figure 3.12 Nyquist plots in a range of temperature (313 K-488 K): a BTO-BT nanocomposite. The inset is exhibiting an enlarged view of the higher frequencies.	94
Figure 3.13 (a) represents plot of the real part of impedance as a function of frequency at different temperatures and (b) Plot of the imaginary part of impedance as a function of frequency at different temperatures for BTO-BT nanocomposite.	95
Figure 3.14 Normalized imaginary part of impedance as a function of frequency for BTO-BT nanocomposite	96
Figure 3.15 (a) AC conductivity with respect to inverse of temperature at different frequencies and (b) Frequency dependent AC conductivity at different temperatures for BTO-BT nanocomposite.	98
Figure 3.16 (a) Dielectric constant (ϵ_r) as a function of frequency and (b) - Dielectric constant (ϵ_r) as a function of temperature for BTO-BT nanocomposite.	99
Figure 3.17 The imaginary part of dielectric constant (ϵ'') as a function of frequency for BTO-BT nanocomposite	101
Figure 3.18 (a) -Dielectric loss ($\tan\delta$) as a function of frequency and (b)- Dielectric loss ($\tan\delta$) as a function of temperature for BTO-BT nanocomposite	103
Figure 3.19 Tauc's Plot for BTO-BT nanocomposite	104
Figure 3.20 N ₂ adsorption-desorption isotherms and the inset corresponding to pore-size distribution curves for BTO-BT nanocomposite	105
Figure 3.21 (a) Absorbance spectra of RhB degradation by BTO-BT, (b) Kinetic plot of RhB degradation by BTO-BT, (c) percentage degradation of RhB with different scavengers.	106
Figure 4.1 HR-XRD patterns of BBTO ceramic sintered at 950 °C for 8 h.	119
Figure 4.2 Le-Bail fitting of BBTO ceramic; black line indicates calculated data, the red line indicates experimental observed data and the blue line represents the difference between observed and calculated ($(Y_{cal} - Y_{obs})$) data.	120
Figure 4.3 FT-IR spectra of BBTO ceramic.	122

Figure 4.4 (a) SAED patterns (b) HR-TEM images showing d spacing, and (c) Bright Field TEM Images of BBTO ceramic.	123
Figure 4.5 (a) SEM micrograph and (b) EDX spectra of BBTO ceramic.	124
Figure 4.6 (a) Histogram graph for the particle size distribution, (b) 3-D for surface roughness and (c) 2-D watershed images for grain boundary of BBTO ceramic.	126
Figure 4.7 Zeta potential distribution of BBTO ceramic	126
Figure 4.8 (a)–(d) High-resolution XPS spectra of the BBTO ceramics.	128
Figure 4.9 (a) M-H hysteresis loop from 5 K to 300 K and (b) Temperature-dependent ZFC and FC at H = 100 Oe for BBTO ceramic.	129
Figure 4.10 (a) represents plot of the real part of impedance as a function of frequency at different temperatures and (b) Plot of the imaginary part of impedance as a function of frequency at different temperatures. (c) Complex impedance spectroscopy in a range of temperature (313 K-488 K) for BBTO ceramic and the inset is exhibiting an enlarged view of the higher frequencies. (d) Normalized imaginary part of impedance as a function of frequency for BBTO ceramic.	131
Figure 4.11 Frequency dependent AC conductivity at different temperatures for BBTO ceramic.	134
Figure 4.12 (a) Dielectric constant (ϵ_r) as a function of frequency; (b) Dielectric constant (ϵ_r) as a function of temperature for BBTO ceramic; (c) Dielectric loss ($\tan\delta$) as a function of frequency; (d) Dielectric loss ($\tan\delta$) as a function of temperature for BBTO ceramic.	136
Figure 4.13 The imaginary part of dielectric constant (ϵ'') as a function of frequency for BBTO ceramic.	138
Figure 4.14 Tauc's Plot for BBTO ceramics.	140
Figure 4.15 N ₂ adsorption-desorption isotherms and the inset corresponding to pore-size distribution curves for BBTO ceramic.	141
Figure 4.16 (a) UV-Vis absorbance spectra of RhB degradation by BBTO photocatalyst, (b) Kinetic first-order kinetic plot for RhB degradation by BBTO, (c) percentage degradation of RhB with different scavengers.	143
Figure 5.1 HR-XRD patterns of BSTO ceramic sintered at 950 °C for 8 h.	155

Figure 5.2 FT-IR spectra BSTO ceramic	156
Figure 5.3 (a) SAED patterns (b) Bright Field TEM Images of BSTO ceramic and (c). HR-TEM images showing d-spacing.	157
Figure 5.4 (a) SEM micrograph and (b) EDX spectra of BSTO ceramic.	158
Figure 5.5 (a) Histogram graph for the particle size distribution, (b) 3-D for surface roughness and (c) 2-D watershed images for grain boundary of BSTO ceramic.	159
Figure 5.6 Zeta potential distribution(a) and particle size distribution(b) of BSTO ceramic.	161
Figure 5.7 (a)–(d) High-resolution XPS spectra of the BSTO ceramics	163
Figure 5.8 (a) M-H hysteresis loop from 5 K to 300 K and (b)Temperature-dependent ZFC and FC at H = 100 Oe for BSTO ceramic.	163
Figure 5.9 Complex impedance spectroscopy in a range of temperature (313 K-488 K) for BSTO ceramic and the inset is exhibiting an enlarged view of the higher frequencies.	164
Figure 5.10 (a) variation of real part of impedance with temperature; (b) variation of imaginary part of impedance with temperature	166
Figure 5.11 Normalized imaginary part of impedance as a function of frequency for BSTO ceramic.	167
Figure 5.12 (a) Dielectric constant (ϵ_r) as a function of frequency; (b) Dielectric constant (ϵ_r) as a function of temperature for BBTO ceramic.	168
Figure 5.13 (a) Dielectric loss ($\tan\delta$) as a function of frequency; (b) Dielectric loss ($\tan\delta$) as a function of temperature for BBTO ceramic.	169
Figure 5.14 Frequency dependent AC conductivity at different temperatures for BSTO ceramic.	170
Figure 5.15 Tauc's Plot for BSTO ceramics.	172
Figure 5.16 N ₂ adsorption-desorption isotherms and the inset corresponding to pore-size distribution curves for BSTO ceramic.	173
Figure 5.17 (a) UV-Vis absorbance spectra of BSTO photocatalyst, (b) UV-Vis absorbance spectra of RhB degradation by BSTO photocatalyst, (c) Kinetic first-order kinetic plot for RhB degradation by BSTO, (d) percentage degradation of RhB with different scavengers	174

Figure 5.18 Recyclability test of BSTO photocatalyst.

176

Table 1.1 Properties of perovskites and their applications	5
Table 1.2 Structure of perovskite oxide based on Tolerance factor (Yadava et al. 2017)	6
Table 1.3 An example of some perovskite explains property application and its use.	14
Table 1.4 Physical properties and applications of some ceramic materials.	16
Table 1.5 Polarization mechanism of dielectric materials	21
Table 1.6 The high dielectric constant of few oxides compound	31
Table 1.7 Various types of magnetic behavior at glance.	34
Table 2.1 Specification of the chemicals used.	54
Table 3.1 Refined lattice parameters and space group of BTO-BT nanocomposite sintered at 900 °C for 8 h.	82
Table 3.2 Data of AFM analysis received for BTO-BT nanocomposite sintered at 900 °C for 8 h	87
Table 3.3 The resistance and capacitance exerted by grain boundaries and grains of BTO-BT nanocomposite.	94
Table 3.4 The value of power-law exponent found for BTO-BT nanocomposite from the plots shown in figure 3.15(b).	99

Table 4.1 Refined lattice parameters and space group of BBTO ceramic sintered at 950 °C for 8 h.	121
Table 4.2 Data of AFM analysis of BBTO ceramic sintered at 950 °C for 8 h.	125
Table 4.3 The resistance and capacitance exerted by grain boundaries and grains of BBTO ceramic at a few selected temperatures.	1133
Table 4.4 The value of power-law exponent found for BBTO ceramic from the plots shown in figure 4.11 at a few selected temperatures.	135
Table 5.1 Data of AFM analysis of BSTO ceramic sintered at 950 °C for 8 h.	159
Table 5.2 The resistance and capacitance exerted by grain boundaries and grains of BSTO ceramic at a few selected temperatures.	166
Table 5.3 The value of power-law exponent found for BSTO ceramic from the plots shown in figure 5.14 at a few selected temperatures.	171

E	Permittivity or dielectric constant
ϵ^*	Complex Quantity of dielectric constant
ϵ'	real components of dielectric constant
ϵ''	Imaginary component of dielectric constant
i	Imaginary number
ϵ_0	Permittivity of free space
ϵ_r	relative dielectric constant
C	Capacitance
F	Farad
$\tan \delta$	tangent loss
σ	conductivity
f	frequency
λ	Wavelength
θ	Angle theta
$^{\circ}\text{C}$	Degree centigrade
K	Kelvin
k_B	Boltzmann constant
T_B	Blocking temperature
χ	Magnetic susceptibility
C	Curie constant
M	Magnetization
H	Magnetic field
Oe	Oersted
ρ	Density

B	Induced magnetic field
E	Electric field
P	Net polarization
P _{electronic}	Electronic polarization
P _{ionic}	Ionic polarization
P _{molecular}	Molecular polarization
P _{interfacial}	Interfacial polarization
Hz	hertz
ω	angular frequency
t	tolerance factor
Å	angstrom
R	Resistance
C	Capacitance
R _b	Resistance of bulk
C _b	Capacitance of bulk
R _{gb}	Resistance of grain boundary
C _{gb}	Capacitance of grain boundary
eV	electron Volt

A surfeit of research work is carrying out on perovskites. The perovskite oxides with the general formula ABO_3 have been widely investigated for their excellent ferroelectric, dielectric, optoelectronic and piezoelectric properties. The materials having high dielectric constant and low dielectric loss has importance in material science due to its applications in electrical and electronic devices such as multilayer capacitor (MLCC), microwave devices, aircraft, dynamic random access memory (DRAMs) and automobiles, gas sensors, capacitors, humidity sensors as well as memory devices. Ceramic capacitor materials sought more attention due to the increasing demand for high dielectric constant and good thermal stability. Thurnauer firstly reported in 1941 the high dielectric constant ($\epsilon_r \sim 10^3$) of $BaTiO_3$ ceramic material but has limitation on temperature dependence of ϵ_r in industrial applications. Further, temperature independent dielectric constant materials have played a significant role in the ceramic capacitor industry. Its easy synthesis, stability in harsh conditions and easily modifiable crystal structure with a series of perovskite family keeps it in demand.

A fundamental understanding of structure-property relationships is imperative in the rational design of new materials for tailored applications. The simple ABO_3 perovskites have been modified to complex perovskite oxide represented by the general formula $(A'A'')(B'B'')O_3$ through doping. The indefinite possibility of configuration and structure of complex perovskite oxides is possible through vast opportunities of doping with homo or heteroatoms, which further open up the chance for a variety of technological applications.

Double perovskite and layered Perovskites are examples of complex perovskite oxide. This research work is focused on layered perovskites. The characteristics feature in the structure of Layered perovskites is the presence of infinite 2D slabs of the simplest ABO_3

perovskite type structure separated by specific motif and layers having the general formula: $A_{(n-1)}B_nO_{(3n+1)}$.

Bismuth-layered perovskite ferroelectric materials belonging to aurivillius oxide semiconductors have lately evoked high curiosity because of their complex layered and unique electronic structure. The Aurivillius phases are composed of alternating layers of $(Bi_2O_2)^{2+}$ units with perovskite-like $(A_{n-1}B_nO_{3n+1})^{2-}$ blocks in between them, where A denotes mono, di- or tri-valent ions (K^+ , Na^+ , Ba^{2+} , Pb^{2+} , Sr^{2+} , Ca^{2+} , Bi^{3+}) and rare earth elements, B represents tetra, penta or hexa valent ions (Ti^{4+} , Ta^{5+} , Nb^{5+} , W^{6+} , Mo^{6+} , etc.) and $m=1, 2, 3, 4, 5$ indicates to the number of BO_6 octahedral amid neighboring $(Bi_2O_2)^{2+}$ layers. The compound thus has polarization in two possible directions in which a small vector along the c-axis switches from the principal direction independently on the a-axis, generating anisotropy and resulting in a high dielectric constant.

This family of materials has fascinated enough owing to its photocatalytic activity in the removal of organic and inorganic pollutants from water and also eradication of bacteria and cancer cells, photoreduction of N_2 or CO_2 as well as acting as photovoltaic material for harvestation of solar energy. The layered arrangement not only allows better polarization of charge species but also provides a better possibility for the diffusion and separation of the photoexcited hole–electron pairs compared to other non-layered photocatalysts. The separation is possible as the reduction and oxidation lattice sites reside in an isolated manner on the edges and faces of the unit ultrathin sheets. The holes generated in the layered photocatalysts are trapped by water molecules present in the interlayer while diffusing to the sheet surface. This accelerated trapping method of holes causes electrons to diffuse easily and efficiently within the unit sheets before getting to the edges of the sheets. Additionally, bismuth (Bi) is a p-block element with a filled d orbital, and the s-orbital of the valence shell (Bi 6s) can hybridize with the p-orbital of

oxygen (O 2p), generating hybridized valence band (VB), which facilitate the mobility of holes in the VB generated by the photons and improves the photocatalytic efficiency of the Aurivillius oxide. Also, the introduction of Bi³⁺ lone pairs on the A site of the aurivillius structure could assist the distortion of perovskite that is responsible for ferroelectricity in the materials

Few physical properties of synthesized Bismuth Layered Aurivillius oxides such as dielectric, impedance, magnetic and hetero-photocatalytic were investigated at selected temperatures and frequencies. A brief description of the research work presented in the thesis, divided into five chapters, is given as follows:

Chapter I gives a brief description of Perovskites, its types and applications. Discussion on Perovskite Structure and Derivatives including cubic perovskites and complex perovskite such as double perovskites and layered Perovskites(Ruddleson-Popper, Aurivillius and Dion-Jacobson phases), A general introduction of ceramic, composite materials, capacitors. An overview of dielectric material and type of polarization present in them along with the dielectric loss and impedance, with discussion on ferroelectric and magnetic properties interaction. Some light has also been shed on heterogeneous photocatalysis, its mechanism and the photocatalysts used in dye degradation. Details of bismuth layered aurivillius oxides and composite materials considered in the current study and the purpose of the thesis is mentioned in this chapter.

Chapter II described the experimental procedure used for the preparation and characterization of the perovskite oxides and their composites. The modified solid state route and the chemical route were used for the preparation of materials. X-ray diffraction(XRD) and transmission electron microscope (TEM) have been studied for the determination of crystalline size and particle size, respectively. Scanning electron

microscope (SEM) and energy-dispersive X-ray spectroscopy (EDX) analysis have been used for microstructural studies and elemental analysis of materials, respectively. The oxidation state of the ceramics was to be examined by X-ray photoelectron spectroscopy, study of surface roughness and the maximum peak height of the materials have been determined by atomic force microscopy (AFM). The mean particle size and distribution, as well as the zeta potential of the material was determined by a dynamic light scattering technique using a Zetasizer Nano-ZS. The Brunauer–Emmett–Teller (BET) surface area was investigated by nitrogen adsorption-desorption isotherm. The magnetic properties of the materials were measured by a superconducting quantum interference device with the temperature and applied field. Dielectric properties of materials were measured on a LCR meter with the variation of temperature and frequency.

Chapter III described the synthesis, characterization $\text{Bi}_4\text{Ti}_3\text{O}_{12}\text{-BaTiO}_3$ (BTO-BT) nanocomposite, a Aurivillius oxide, which is synthesised by modified solid-state route, and characterised by various techniques like FTIR, XRD, TEM, UV-DRS, Zetasizer Nano-ZS, AFM, BET, SEM-EDX and XPS for the phase identification, microstructural analysis, bandgap determination, elemental analysis and oxidation state of the material. Formation of BTO-BT nanocomposite (orthorhombic and cubic) confirmed by Le-Bail fitting analysis with the help of XRD data. The electrical measurement of the material showed the existence of semiconducting grains and insulating grain boundaries responsible for Maxwell relaxation and a high dielectric constant of value 4.75×10^3 at 368 K was observed. The Magnetic behavior studied by SQUID indicates it to be magnetically frustrated materials. The material was found to be applicable in photocatalytic degradation of Rhodamine B under UV light through major reactive species, i.e. OH^\cdot radicals and $\text{O}_2^{\cdot-}$ generated during the photocatalytic reaction proved to be following the first-order kinetics.

Chapter IV contains $\text{Bi}_4\text{BaTi}_4\text{O}_{15}$ (BBTO), an Aurivillius oxide, which is mixed metal bismuth-layered based oxide fabricated by chemical route, has shown highly efficient photocatalytic activity in degradation of organic dye besides possessing high dielectric constant. The obtained material was characterised by various techniques like Fourier Transform Infrared (FTIR), transmission electron microscope, Scanning Electron Microscopy-Energy Dispersive X-rays Spectroscopy (SEM-EDX) X-ray powder diffraction (XRD), Zetasizer Nano-ZS, Ultraviolet- differential reflectance spectroscopy (UV-DRS), Brunauer-Emmett-Teller, Atomic Force Microscopy (AFM) and X-ray photoelectron spectra for the phase identification, microstructural analysis, bandgap determination, elemental analysis and oxidation state of the material. XRD data confirm the presence of single-phase BBTO ceramic, corroborated by Le-Bail fitting analysis. A high dielectric constant value of 3.08×10^3 was obtained for the BBTO ceramic at 368 K. The material is stable in suspension form in solution and is a highly efficient photocatalyst. BBTO degraded 80% of RhB dye within 1 h of time period under UV light via major reactive species OH^\cdot radicals and $\text{O}_2^\cdot-$, generated during the photocatalytic reaction, which is proved to be following the first-order kinetics.

Chapter V contains $\text{Bi}_4\text{SrTi}_4\text{O}_{15}$ (BSTO), which is mixed metal bismuth-layered based Aurivillius oxide synthesized by the chemical route. Besides possessing high dielectric constant, it also shows much efficient photocatalytic activity in the degradation of organic dye. The obtained material was characterized by various techniques like Fourier Transform Infrared (FTIR), transmission electron microscope (TEM), Scanning Electron Microscopy-Energy Dispersive X-rays Spectroscopy (SEM-EDX) X-ray powder diffraction (XRD), Zetasizer Nano-ZS, Ultraviolet- differential reflectance spectroscopy (UV-DRS), Brunauer-Emmett-Teller, Atomic Force Microscopy (AFM) and X-ray photoelectron spectra for the phase identification, microstructural analysis,

bandgap determination, elemental analysis and oxidation state of the material. XRD data confirm the presence of single-phase BSTO ceramic. A high dielectric constant value of 2.76×10^3 was obtained for the BSTO ceramic at 368 K. The material is stable in suspension form in solution and is a highly efficient photocatalyst. BSTO degraded 84% of RhB dye within 1 h of the time period under UV light via major reactive species OH· radicals and O₂⁻, generated during the photocatalytic reaction, which is also proved to be following the first-order kinetics.